Mass transport and active area of porous Pt/Ti electrodes for the Zn-Ce redox flow battery determined from limiting current measurements

L.F. Arenas [a, ‡], C. Ponce de León [a], F.C. Walsh [a,*]

[a] Electrochemical Engineering Laboratory, Energy Technology Group, Faculty of Engineering and the Environment, University of Southampton SO17 1BK, UK.

* Author for correspondence: F.C. Walsh; F.C.Walsh@soton.ac.uk

‡ E-mail: lfam1g13@soton.ac.uk

Abstract

The conversion of soluble cerium redox species in the zinc-cerium redox flow battery and other electrochemical processes can be carried out at planar and porous platinised titanium electrodes. The active area, current density, mass transfer coefficient and linear electrolyte flow velocity through these structures have a direct influence on the reaction yield and the relationship between cell potential and operational current density during charge and discharge of a flow battery. A quantitative and practical characterization of the reaction environment at these electrodes is required. The volumetric mass transfer coefficient, $k_m A_e$ has been calculated from limiting current measurements for Ce(IV) ion reduction in a laboratory, rectangular channel flow cell. This factor can be used to predict fractional conversion and required electrode dimensions. Highly porous platinised titanium felt shows superior $k_m A_e$ values and is well-suited as a high performance electrode material.

Keywords: cerium, energy storage, felt, platinum, porous electrodes, redox flow battery, titanium. (Approx. 10,000 words, 4 tables, 8 figures, 13 equations/reactions and 60 references).

1. Introduction

The zinc-cerium redox flow battery (Zn-Ce RFB) has been the subject of semicontinuous development over the past decade; its progress and research challenges have been recently reviewed [1,2]. Its main advantages are a higher standard cell potential (2.48 V) and lower electrolyte toxicity than all-vanadium or Zn-Br_2 RFBs. Diverse electrode materials have been studied for both positive [3,4] and negative [5,6] electrode reactions as well as alternative electrolyte compositions [7-10]. The inhibition of hydrogen evolution as a secondary reaction, or via open-circuit corrosion, at the zinc negative electrode by electrolyte additives has also been considered [11]. In previous work [12], we have shown the contribution of thermodynamic, kinetic and ohmic components to the cell potential losses in the Zn-Ce RFB, evaluating the effect of electrolyte conductivity and interelectrode gap. Other cerium-based RFBs have been proposed, including: a Ce-Ce concentration cell [13], an undivided Zn-Ce RFB [7,14], a V-Ce RFB [15-19], a borohydride-Ce fuel cell [20], a Pb-Ce RFB [21] and a H_2-Ce fuel cell [22-24].

Cerium-based RFBs involve reduction of Ce(IV) ions at the positive electrode during discharge, usually in aqueous methanesulfonic acid (MSA), with the reverse process during charge:

$$\mathrm{Ce(IV)} + \mathrm{e^-} \underset{\text{Charge}}{\overset{\text{Discharge}}{\rightleftarrows}} \mathrm{Ce(III)} \qquad E^{\ominus} = +1.74\ \text{V } \textit{vs.}\ \text{SHE} \qquad (1)$$

Platinised titanium (Pt/Ti) is a suitable electrode material for this reaction due to its catalytic activity for cerium conversion together with its stability to highly oxidising Ce(IV) ions [1]. The positive electrode also supports the oxygen evolution reaction (OER) as a secondary reaction during anodic Ce(III) oxidation:

$$H_2O \xrightarrow{\text{Charge}} \frac{1}{2}O_{2\,(g)} + 2H^+ + 2e^- \qquad E^{\Theta} = +1.23\ \text{V}\ \textit{vs.}\ \text{SHE} \qquad (2)$$

This results in a lower current efficiency for reaction (1), especially at high current densities on planar electrodes or under low mass transport conditions. Porous, 3-D electrodes can reduce these limitations by decreasing the local current density and increasing the mass transport rate of Ce(IV) ions to the electrode surface. Enhanced electrolyte flow through these materials also helps prevent electrode shielding by gas bubbles and ohmic losses due to gas voidage in the electrolyte. The extended surface area of porous electrodes enables a faster conversion rate of active species.

Despite the common use of Pt/Ti mesh in cerium-based RFBs and other electrochemical reactors, no quantitative or comparative studies have been undertaken on the reaction environment at diverse Pt/Ti electrode structures for cerium ions. Here, the quantitative performance of such Pt/Ti porous electrode materials is expressed as the volumetric mass transport coefficient $k_m A_e$ (the product of mass transport coefficient and electroactive volumetric electrode area) derived from dimensionless group analysis as a function of the electrolyte flow rate and associated flow characteristics. Assuming plug-flow and convective-diffusion control, $k_m A_e$ allows the fractional conversion of the active species, X_A, to be predicted as well as the electrode dimensions and maximum operational current for an acceptable potential loss [25]. In this way, cost-effective materials can be found and further insight into the dynamic relationship between the operational cell potential, current density and the reaction environment at the different electrode materials/structures can be provided.

The performance factor $k_m A_e$ was determined from limiting current measurements for Ce(IV) ion reduction in half-cell experiments. Few studies have considered the experimental reaction environment in RFBs from the perspective of dimensionless group analysis, which can be an

important step in the scale-up of electrochemical technology [26]. Such an approach allows laboratory and pilot-scale flow cells as well as different electrode materials (including carbon felt under different degrees of compression in all-V RFBs) to be compared. As discussed in a recent review [27], the performance of Pt/Ti electrodes is also important to diverse industrial electrochemical processes reliant on anodic generation of Ce(IV). Electrode optimization is desirable to increase space-time yield and minimize electrolyte material, electrolytic cell potential and energy consumption.

2. Theoretical Considerations

2.1. Cell geometry and flow expressions

The characteristics of a rectangular flow cell required for mass transport characterization include: equivalent (hydraulic) diameter, d_e dimensionless length group, Le and the aspect ratio of the channel, γ. These are defined as:

$$d_e = \frac{2A_x}{B+S} \tag{3}$$

$$Le = \frac{d_e}{L} \tag{4}$$

$$\gamma = \frac{S}{B} \tag{5}$$

where B, S and L are the breadth, span, and length of the channel, respectively, and A_x is the cross sectional area ($A_x = BS$). The relationship between the mean linear electrolyte flow velocity, v [cm s^{-1}] and the volumetric flow rate, Q [cm^3 s^{-1}] through a rectangular channel of uniform volumetric porosity, ε and cross-sectional area, A_x is given by:

$$v = \frac{Q}{\varepsilon A_x} \tag{6}$$

2.2. Dimensionless group correlations

The mass transport characteristics in a uniform cross-section, rectangular channel electrochemical flow cells can be described by the dimensionless group correlation [25,28]:

$$Sh = aRe^{b}Sc^{1/3} \tag{7}$$

Sh is the Sherwood number, Re is the Reynolds number, Sc is the Schmidt number and a and b are empirical constants. These dimensionless groups are defined as:

$$Sh = \frac{k_m d_e}{D} \tag{8}$$

$$Re = \frac{v d_e}{\nu} \tag{9}$$

$$Sc = \frac{\nu}{D} \tag{10}$$

k_m is the mass transport coefficient, D is the diffusion coefficient of the active species, and ν is the kinematic viscosity of the electrolyte. The characteristic length used in this work is the equivalent or hydraulic diameter of the channel, d_e.

2.3. The electrode performance factor $k_m A_e$

Under mass transport controlled reaction conditions, the performance of porous electrodes can be expressed using the factor, $k_m A_e$, i.e., the product of the average mass transport coefficient, k_m, and volumetric electrochemical area, A_e [25,28,29]. These variables are often considered as a product in view of the experimental difficulties in the determination of their individual values in flow cells containing practical electrode structures. For instance, it is known that the

surface area determined by BET is much higher than the real electrochemical active area [30], while the geometrically calculated surface area often results in conflicting results when k_m is estimated from the limiting currents measured with different redox couples, e.g., ferricyanide/ferrocyanide-bromine/bromide for a RFB cell [31] or ferricyanide/ferrocyanide-Hg(II)/Hg for carbon felt [32]. The performance factor $k_m A_e$ can be determined in two ways: a) from the limiting current achieved at the electrodes or b) by following the conversion rate of the active species as described by a plug-flow reactor model [25,28]. Mass transport rate control is assumed in both cases. In this work, the limiting current method is used for simplicity, convenience and speed.

The volumetric mass transport coefficient $k_m A_e$ is obtained from the dimensionless groups by expanding Equation (7) and multiplying it by the volumetric active electrode area, A_e. Further rearrangement allows $k_m A_e$to be expressed as a function of the electrolyte mean electrolyte flow velocity, v. If the other variables are grouped as the constant a', $k_m A_e$ can be expressed in the form of an empirical power law:

$$k_m A_e = a' v^{b'} \tag{11}$$

The values of a' and b' can then be used to quantitatively characterize different electrodes. Approximate k_m values and other empirical correlations (such as Sh *vs.* Re relationships) can be obtained directly from Equation (7) once A_e is known.

The relationship between $k_m A_e$ and the limiting current for Ce(IV) ion reduction at the porous electrode I_L is:

$$k_m A_e = \frac{I_L}{zFcV_e} \quad (12)$$

V_e is the volume of the electrode channel, z is the number of electrons involved in the written reaction, F is the Faraday constant and c the bulk concentration of the reactant. Alternatively, the mass transport coefficient in a batch electrochemical reactor for cerium conversion has been estimated from measurements of reactant conversion over time [33]. A similar approach was used to determine the average k_m in a pilot-scale bromine-polysulfide RFB [26].

The limiting current enhancement factor, β expresses the ratio of limiting current in a porous material, I_L, compared to a planar electrode, $I_L{}'$:

$$\beta = \frac{I_L}{I_L{}'} \quad (13)$$

Under full convective-diffusion control and equivalent mass transport, β reflects the relationship between the active area of the porous electrode, $A_e V_e$ and the active area of a planar electrode, A.

The limiting current in mass transport studies has been classically measured using reversible reactions such as the reduction of ferricyanide ions, e.g., [34], or Cu^{2+} ions, e.g., [35]. However, it is important to consider the electrode/electrolyte conditions used in Ce-based RFBs and the present study uses Pt/Ti in a MSA electrolyte containing Ce(IV) ions at typical concentrations. In other cases, limiting currents have been determined directly from the reduction of Ag^+ ions [36] and O_2 [37]; the determined mass transport coefficients are characteristic for the

electroactive species and electrolyte composition (and associated physical properties, e.g., viscosity) [32].

3. Experimental

3.1. Electrolytes

Half-cell limiting current, voltammetry and charge-discharge experiments were performed using electrolytes for the Zn-Ce RFB: 0.8 mol dm^{-3} Ce(III) methanesulfonate in 4.0 mol dm^{-3} MSA (positive electrolyte) and 1.5 mol dm^{-3} Zn(II) methanesulfonate in 1.0 mol dm^{-3} MSA (negative electrolyte). Methanesulfonate solutions were prepared by neutralizing hydrated cerium carbonate (99% purity, Treibacher Industrie AG, Austria) and basic zinc carbonate (97% purity, Alfa Aesar, UK) with stoichiometric volumes of MSA (99% purity, Acros Organics, USA). Excess MSA was added to reach the required acid concentration. The concentration of cerium was determined by volumetric titration against Fe(II) using ferroin (1,10-phenanthroline-ferrous sulfate) as indicator [38]. Deionized water of 4.5 μS cm^{-1} conductivity was used throughout. The viscosity of the positive electrolyte was measured with an Oswald viscometer. The properties of the electrolyte used in the limiting current measurements are summarized in Table 1.

3.2. Flow cell and electrolyte recirculation

All electrodeposition, limiting current and charge-discharge experiments were performed in the rectangular channel flow cell shown in Figure 1a). The flow compartments were manufactured in acrylic polymer by CNC machining, interchangeable electrodes with geometrical areas of 24 to 26 cm^2 being used. The flow frames had a thickness of 2.75 mm, except for the Pt/Ti mesh electrode, where the flow frame had a thickness of 6.5 mm. The half-cells were divided by a Nafion® 115 (Dupont Co, USA) proton exchange membrane and its components were separated

by 0.5 mm (*ca.* 0.4 mm compressed) thick silicone gaskets (PAR Group Ltd, UK) held together by mechanical compression.

The experimental arrangement for half-cell measurements of limiting current is shown in Figure 1b). A three-electrode cell configuration was used and the experiments were performed using an Autolab digital potentiostat connected to a 20 A booster (Metrohm AG, The Netherlands). The Pt/Ti electrodes were connected to the working electrode terminal and the electrode potential was measured *vs*. a $Hg|Hg_2SO_{4(satd)}$ reference electrode with the aid of a Luggin capillary inserted through the corresponding acrylic cell frame. A Pt/Ti plate or graphitized polymer was used as counter-electrode and its flow channel contained inert turbulence promoters (ITP). Electrolyte recirculation was performed with two Masterflex L/S (Cole-Parmer Co, USA) peristaltic pumps. Pressure pulse dampeners were incorporated in the hydraulic circuit to supress pulsating flow. The electrolyte reservoirs with water jackets were connected to a thermostatic water bath in order to control temperature to within ±0.5 K.

The experimental arrangement for charge-discharge experiments was similar, but in this case the flow cell was connected to a BST8-A3 battery analyser (MTI Corp., USA) and 100 cm^{-3} reservoirs were used for both positive and negative electrolytes. An additional reference electrode measured the electrode potential of the negative electrode, which consisted of a 5 mm thick graphitized fluorocarbon polymer-composite, Sigracet® BMA5 plate (SGL Carbon GmbH, Germany). Its area was limited to 60 mm × 40 mm and it was connected to a 2.3 mm thick copper plate current feeder of the same dimensions. In order to ensure effective electrical contact, the electrode and current collector were bonded with a cured silver-loaded epoxy resin, (Circuitworks, Chemtronics, USA). The negative flow channel contained the same turbulence

promoters in order to maintain a constant electrode-membrane gap. The flow system for Pt electrodeposition is described in the following section.

3.3. Preparation of electrodes

The evaluated positive electrodes are shown in Figure 2 and their characteristics are given in Table 2. The Pt/Ti plate and Pt/Ti mesh electrodes were ordered from a commercial supplier (Magneto Special Anodes BV, The Netherlands), while the fine Pt/Ti mesh and Pt/Ti felt were constructed from commercially available Ti materials and platinised in-house. The porosity of the plate + ITP and mesh electrodes was determined by measuring the internal void volume with a liquid of known density. In the case of the Ti felt, porosity was measured gravimetrically. SEM images were taken on a JSM-6500F field emission electron microscope (Jeol Inc, USA).

The Pt/Ti plate electrode consisted of a 3 mm thick titanium sheet. The flow channel containing three stacked inert polypropylene meshes (internal aperture 4.6 × 4.2 mm, pitch 6.8 × 8.0 mm, thickness 1.3 mm) as ITP between the Pt/Ti sheet and the membrane. The mesh electrode consisted of a stack of three identical, expanded titanium meshes (internal aperture 3.2 × 7.1 mm, pitch 6.8 × 10.1 mm, thickness 2.4 mm) spot-welded to a titanium plate forming a 60 × 42 × 7.4 mm porous electrode including the flat area next to the mesh. In both cases, the externally supplied platinum coating had a nominal thickness of 3.5 μm, with an approximate platinum loading of 7 mg cm^{-2}.

The Pt/Ti micromesh electrode was formed from sixteen, identical 60 × 25 mm flat titanium meshes (each of internal aperture 375 × 625 μm, pitch 670 × 1000 μm, thickness 170 μm) (Dexmet Co., USA) spot-welded to a 0.9 mm thick 99.7% Ti plate (Alfa Aesar Ltd., UK). The individual pieces of mesh, which have a smaller breadth than the overall electrode, were stacked

alternately with strips of mesh (60 × 5 mm) to leave space for the flowing electrolyte and to form a 60 × 40 × 2.5 mm porous electrode. Sintered titanium fibre (NV Bekaert SA, Belgium), commonly used in water electrolysers, was used for the Pt/Ti felt electrode. The fibres had irregular rectangular-like cross-sections with a maximum average side length of 42.3±4.4 μm. The rigid bulk material had an average density of 0.88 g cm^{-3} and a volumetric porosity, ε, of 0.80. The thickness of the felt was 3.6 mm, resulting in an electrode having dimensions 60 mm × 40 mm × 3.6 mm. The felt was spot-welded to a Ti plate at several sites to ensure an effective electrical contact.

The Pt/Ti micromesh and felt electrodes were platinised in a flowing aqueous, alkaline electrolyte using the cell in Figure 1a). Firstly, a flow-only configuration was adopted for the chemical etching of the Ti substrates using a 10% volume/weight oxalic acid solution at 353.2 K until a dark brown colouration was developed [39]. The etching solution was removed and the system was triply cleaned with deionized water. A divided cell configuration was later adopted using a Nafion® ion exchange membrane and a planar Pt/Ti electrode as anode. A 50 cm^3 volume of the platinising solution containing 20 g dm^{-3} hexachloroplatinic (IV) acid (Fischer Scientific Ltd., UK) in 0.1 mol dm^{-3} NaOH solution (pH 13) [40] was recirculated in the cathodic half-cell at a mean linear flow velocity of 8 cm s^{-1} past the electrode surface, maintaining a temperature of 348.2 K. The anodic half-cell contained 0.1 mol dm^{-3} NaOH. Pt electrodeposition was performed at a constant potential of –0.2 V *vs.* $Hg|HgO_{(satd)}$. The procedure was stopped after the yellow colour of the solution disappeared and significant hydrogen evolution was observed. The total consumption of dissolved Pt was confirmed by tin(II) chloride and potassium iodide in spot tests on the residual solution [41].

The first electroplating of Ti felt, referred to as 'Pt/Ti felt A', did not result in a satisfactory Pt coverage. Therefore, the Pt/Ti felt A was platinised a second and a third time, using 50 cm^3 and 100 cm^3 of the Pt solution, the resulting electrodes being referred to as 'Pt/Ti felt B', and 'Pt/Ti felt C', respectively. The change in porosity with increasing Pt loading was found to be negligible. During these stages, the treatment with oxalic acid was extended to 4 hours in view of the time required to observe a change in colouration. This was followed by additional chemical etching at the same temperature in 6.0 mol dm^{-3} HCl for 1 hour and in 1.0 mol dm^{-3} aqueous H_2O_2 for 0.5 hour. The second and third electroplating procedures were performed galvanostatically at 100 mA cm^{-2} until the consumption of dissolved Pt was verified. The distribution and coverage of platinum in the Pt/Ti micromesh and Pt/Ti felt electrodes is subject of discussion in a related work [42].

3.4. Electrochemical experiments

3.4.1. Cycling voltammetry and rotating disc experiments

The electrochemical response for cerium ions in an electrolyte containing 0.8 mol dm^{-3} Ce(III) in 4.0 mol dm^{-3} MSA was assessed by cyclic voltammetry at a Pt disc electrode and the diffusion coefficient of the Ce(IV) ions was calculated by the limiting current technique using the Levich equation. A typical 150 cm^{-3} three-electrode cell connected to an Autolab digital potentiostat (Metrohm AG, The Netherlands) was used for this purpose. The cyclic voltammetry was performed from 0 to +1.5 V *vs.* $Hg|Hg_2SO_{4(satd)}$ at a linear potential sweep rate of 20 mV s^{-1}. The linear sweep voltammetry for the Levich study was performed from –0.6 to +1.0 V *vs*. $Hg|Hg_2SO_{4(satd)}$ at a scan rate of 5 mV s^{-1}. Rotation rates varied between 100 and 2025 rpm. The reduction of Ce(IV) ions, instead of the oxidation of Ce(III), was studied in order to avoid parasitic currents due to OER.

3.4.2. Battery discharge polarisation curve

The cell potential of the flow battery as a function of discharge current density (cell polarisation) was measured for each electrode material in a Zn-Ce cell. The positive and negative electrolytes consisted of 0.8 mol dm^{-3} Ce(III) methanesulfonate in 4.0 mol dm^{-3} MSA and of 1.5 mol dm^{-3} Zn(II) methanesulfonate in 1.0 mol dm^{-3} MSA. Volumes of 100 cm^{-3} were used of each electrolyte. Increasing electrolyte flow rates were evaluated in the positive half-cell while the Zn negative electrolyte was maintained at 4 cm s^{-1} in all cases. Each cell potential value was recorded after 60 s at the specified current density. The experiments were carried out at the typical operative temperature of 323.2 K [1] after charging the battery to a state of charge (SOC) of 50%, equivalent to 0.4 mol dm^{-3} Ce(IV).

3.4.3. Linear sweep voltammetry (LSV)

Electrode polarization curves for the reduction of Ce(IV) ions were recorded in half-cell studies using linear sweep voltammetry (LSV). As shown in Figure 1b), the positive half-cell reservoir contained 1.3 dm^3 of positive electrolyte with 0.1 mol dm^{-3} Ce(IV) methanesulfonate and 0.7 mol dm^{-3} Ce(III) methanesulfonate in 4.0 mol dm^{-3} MSA. A planar Pt/Ti or graphitized polymer counter-electrode was used and the negative half-cell reservoir contained 0.1 dm^3 of a zinc-free 4.0 mol dm^{-3} MSA solution. The electrolyte flow rates were digitally controlled and the temperature of the electrolyte was maintained at 298.2 K.

For the planar and mesh electrodes, LSV was performed from –0.6 to +0.90 V *vs.* $Hg|Hg_2SO_{4(satd)}$ at 5 mV s^{-1}. The LSV for Pt/Ti felts was carried out from –0.2 to +0.90 V *vs.* $Hg|Hg_2SO_{4(satd)}$ to avoid hydrogen evolution, which shifted to higher potentials due to the great surface area and catalytic activity of the Pt deposits. Before these experiments, the

electrochemical response of the Pt/Ti felt electrodes was stabilized by performing 120 voltammetric cycles from –0.2 to +1.2 V *vs.* $Hg|Hg_2SO_{4(satd)}$ at 1 V s^{-1}.

3.4.4. Chronoamperometry

The limiting current at the positive electrodes was measured by chronoamperometry for convenience and to minimize the change in Ce(IV) concentration (0.1 mol dm^{-3}) in the 1.3 dm^{-3} volume of electrolyte. The cell configuration and temperature were the same as in the LSV measurements (Figure 1b). A potential of +0.2 V *vs.* $Hg|Hg_2SO_{4(satd)}$ was imposed with the potentiostat and the current was recorded during successive steps of increasing flow rate performed every 30 s, except for the micromesh and the felt, when the interval was 15 s. The values used in data analysis were an average of the current recorded during the last 10 s of each step taken from triplicate measurements. The change in Ce(IV) concentration over the duration of each experiment was <1% with the plate and mesh electrodes and <5% for the micromesh and felt electrodes, hence the shorter intervals between flow rate steps.

4. Results and Discussion

4.1. Electrode material and structure

SEM images of the macroscopic structure and Pt coverage of the electrode materials are shown in Figure 3. Both Pt/Ti plate (Figure 3a) and Pt/Ti mesh (Figure 3b) have uniform, compact Pt coatings with a roughened appearance. The individual pieces of micromesh in the Pt/Ti micromesh stack adjacent to the membrane during electrodeposition, are predominantly covered with Pt (Figure 3c). It can be observed that nodular growths are sparsely distributed throughout it. The uneven coverage in the first layer of micromesh might be the result of the physical blockage of the substrate during the etching step. The outer surface (next to the membrane) of the Pt/Ti felt C is characterized by numerous Pt nodules, of 40-45 μm

approximate diameter, that grow over the length of the fibres, covering them entirely (Figure 3d). In contrast, the outer individual fibres in the exterior of the Pt/Ti felt A were incompletely covered with Pt (not shown), while those in the Pt/Ti felt B presented a higher density of Pt nodules fused together (not shown).

The distribution of Pt in the interior of the highly porous Pt/Ti micromesh and Pt/Ti felt electrodes is non-homogeneous due to the changes in the potential and current distributions at both electrode material and electrolyte during electrodeposition [42]. However, a space-averaged volumetric Pt loading can be calculated for comparison purposes from the total volume of each electrode and the mass fraction of platinum in hexachloroplatinic(IV) acid, *ca*. 40%. The Pt volumetric loading of the micromesh electrode was 6.4 mg cm^{-3}. The increasing Pt content in the felt electrode through the three electroplating steps, is reflected in the volumetric loading. The estimated Pt volumetric loading of the Pt/Ti felt A, Pt/Ti felt B and Pt/Ti felt C electrodes was 4.6 mg cm^{-3}, 9.3 mg cm^{-3}, and 18.3 mg cm^{-3}, respectively.

4.2. Cyclic voltammetry and rotating disc experiments

The cyclic voltammetry in Figure 4 illustrates the overall redox behaviour of cerium ions in typical electrolytes used in the Zn-Ce RFB. The oxidation of Ce(III) ions overlaps with oxygen evolution at potentials near +1.1 V *vs.* $Hg|Hg_2SO_{4(satd)}$ and increases at more positive potentials. The current peak for the oxidation of Ce(III) can be found near +1.26 V *vs*. $Hg|Hg_2SO_{4(satd)}$ while the current peak corresponding to the reduction of Ce(IV) is located near +0.58 V *vs.* $Hg|Hg_2SO_{4(satd)}$. The peak separation is approximately 0.68 V. These results are similar to those reported in other MSA-based electrolytes for the Zn-Ce battery [43].

The diffusion coefficient of Ce(IV) at a concentration of 0.1 mol dm^{-3} (see Table 1) was determined using the Levich equation from well-developed cathodic limiting current plateaus for 0.1 mol dm^{-3} Ce(IV) in the industrial/RFB composition electrolyte at the Pt RDE (not shown). This value is comparable to those found in the literature; a diffusion coefficient of 1.0 × 10^{-6} cm^2 s^{-1} was reported for Ce(III) ions MSA industrial electrolytes [44,45]. To put this in perspective, at a lower concentration of 0.01 mol dm^{-3} the diffusion coefficient of Ce(IV) ions in 3.0 mol dm^{-3} sulfuric acid is 2.5 × 10^{-6} cm^2 s^{-1} [46].

4.3. Operational cell potential as a function of discharge current density

Cell polarization curves showing the effect of electrolyte flow rate at the positive electrode in a Zn-Ce battery are presented in Figure 5. The E_{cell} is presented as a function of increasing discharge current density under galvanostatic control at different flow rates for each of the positive electrode structures. The materials behave as resistive systems except for the Pt/Ti plate or at flow rates cero or lower than 2.8 cm s^{-1} for the Pt/Ti-mesh. They also have different ability to maintain a high operational E_{cell}, and different response to increasing electrolyte flow rate. The fact that the observed potential drops due to mass transport limitation took place predominantly at the positive electrode, was confirmed by measuring the individual electrode potentials of each half-cell reaction.

Figure 5a) shows that the E_{cell} of the planar electrode drops substantially from 2.37 V to 0.62 V after applying a current density of 10 mA cm^{-2} at a linear flow velocity of 4 cm s^{-1}, corresponding to an area-specific resistance of 20.7 Ω cm^2. (The area-specific resistance, R_A, is the normalized electrical resistance of a cell with a projected area of A: $R_A = R_{cell}A$. The cell resistance, R_{cell}, is calculated from the potential loss: $\Delta E = IR_{cell}$.) This resistance is in same range as that reported for a Zn-Ce RFB with planar electrodes operating at a linear flow velocity

of 12 cm s^{-1} (50 Ω cm^2) [47]. Increasing the electrolyte flow rate to 17 cm s^{-1} had little effect on reducing the potential drop, as implied by its low $k_m A_e$. Nevertheless, the potential loss at these planar electrodes appears to be the result of the OER. Small bubbles, are observed in the positive half-cell during the battery charge and in larger quantities during discharge. Bubbles can produce significant ohmic drops in flow reactors by increasing the resistivity of the electrolyte [48] and by shielding the electrode surface [49]. This would be consistent with the fact that no large potential losses were predicted for an ideal Zn-Ce model cell with planar electrodes under the assumption of no OER [12]. Consistently, a steep fall in current efficiency with increasing current density due to the OER was observed during Ce(III) oxidation in sulfuric acid at dished planar electrodes [50].

In contrast to the planar electrode, the cell polarization for the Pt/Ti mesh electrode reveals a much lower effect of concentration overpotential and ohmic loss due to OER, as shown in Figure 5b). Under static electrolyte conditions, E_{cell} losses are actually lower than those experienced by the planar electrode at a linear flow velocity of 17 cm s^{-1}. The behaviour of the mesh provides an illustrative example of the effect of mass transport in a flow cell. Although the potential drop is significant at low electrolyte flow rates, E_{cell} develops higher values as the mean linear flow rate in the cell is increased to 8.5 cm s^{-1}, due to a reduction in the concentration overpotential. The resulting linear fall in E_{cell} from 2.37 V at E_{cell}^{OC} to 1.62 V at 100 mA cm^{-2} (corresponding to an area-specific resistance of 7.5 Ω cm^2) is consistent with kinetic and ohmic losses similar to those observed in another Zn-Ce RFB with a mesh electrode (corresponding to an area-specific resistance of 9.2 Ω cm^2 at 50 mA cm^{-2}) [3]. E_{cell} values over 1.5 V at a current density of 80 mA cm^{-1} are observed in the RFB cell over a mean linear electrolyte velocity of 2.8 cm s^{-1}, under conditions that would detach bubbles from the electrode surface and maintain good mass transport rates.

The E_{cell} *vs*. j relationship for the micromesh electrode is presented in Figure 5c). Concentration overpotential losses occur only when there is no electrolyte flow and a linear decay in E_{cell} consistent with ohmic loss predominance is developed even at the lowest flow rate of 0.25 cm s^{-1}, with insignificant change at increasing flow rates. This implies that the surface area and mass transport in the micromesh are high enough to minimize concentration overpotential and local current density. The slope of E_{cell} *vs*. j is steeper than the case of the mesh electrode, indicating higher ohmic resistivity in the cell (an area-specific resistance of 11.2 Ω cm^2 at 100 mA cm^{-2}). The electrical resistance of all electrode/current collector assembles and their electrical connections was < 1 mΩ, therefore it cannot account for this loss. In view of the area-specific resistance of Nafion® being 0.13 Ω cm^2 [51], ohmic resistance lies at the electrolyte. The behaviour of the battery with the Pt/Ti felt C electrode in Figure 5d) is similar to that of the micromesh electrode, although ohmic loses are considerably lower. E_{cell} decreases from 2.36 V at E_{cell}^{OC} to 1.20 V at 100 mA cm^{-2} at a mean linear flow velocity of 1 cm s^{-1} (an area-specific resistance of 6.8 Ω cm^2).

The polarization curves for these cells can be compared to those obtained from other RFBs. For instance, The overall behavior an all-vanadium RFB was similar to the Zn-Ce RFB, showing a linear E_{cell} decrease dominated by ohmic components [52]. The area-specific resistance at 152 mA cm^{-2} was 4.6 Ω cm^2 at an estimated flow rate of 5 cm s^{-1} (the authors did not provide clear electrode dimensions or a mean linear flow rate). The resistance of the vanadium flow cell can be decreased by using serpentine flow fields and carbon paper to 0.66 Ω cm^2 [52]. In the case of bromine-polysulfide RFB cell with nickel foam electrodes the cell area-specific resistance is comparatively much lower [53]. E_{cell} decreased from 1.5 V at E_{cell}^{OC} to 1.25 V at 500 mA cm^{-2} (area-specific resistance of 0.5 Ω cm^2) at an electrolyte flow rate of 0.5 cm^3 s^{-1} (the authors did

not provide the electrode dimensions or a mean linear flow rate). In [52] and [53] thinner electrodes showed increased rates of mass transport and allowed operation at higher current densities, suggesting that thin felt electrodes (e.g., <500 μm) should be used in the Zn-Ce cell. In summary, the contribution of ohmic components is predominant in Zn-Ce and other RBFs, provided mass transport conditions that avoid concentration polarisation.

4.4. Polarization curves and chronoamperometry of Pt/Ti electrodes

Polarization curves of the different electrode materials were obtained with the purpose of selecting a suitable electrode potential value to perform chronoamperometry measurements of limiting current. Figures 6a) and 6b) illustrate this approach with the case of Pt/Ti plate electrodes. Insignificant variation was found between the limiting currents measured via LSV and later chronoamperometry when using the Pt/Ti plate and mesh electrodes. For the Pt/Ti felts the LSV the current differed at most by 4% from that measured by chronoamperometry at the imposed potential. The limiting current region at Pt/Ti planar electrode started at a potential close to +0.2 V *vs.* $Hg|Hg_2SO_{4(satd)}$. This potential value was chosen for the chronoamperometry experiments shown in Figure 6b) and the same potential was used with the other electrodes for consistency. In these experiments, limiting currents were measured as the electrolyte mean linear flow rate was increased in steps.

Limiting current plateaux are obtained with the Pt/Ti planar electrode (Figure 6a). The initial high current observed with the electrode at –0.6 V *vs.* $Hg|Hg_2SO_{4(satd)}$ corresponds to double layer charging, rather than to H_2 evolution. The onset potential for this reaction was intentionally avoided. H_2 evolution was observed at *ca.* –0.4 V *vs.* $Hg|Hg_2SO_{4(satd)}$ at the micromesh electrode, while the felt electrodes displayed an intense catalytic activity towards

H_2 evolution due to the large surface area of the Pt catalyst at a potential of –0.2 V *vs.* $Hg|Hg_2SO_{4(satd)}$.

The polarization curves for Ce(IV) ion reduction at high-surface area electrode materials, such as Pt/Ti micromesh and Pt/Ti felt displayed a less ideal behaviour due to a combination of a) deviation from steady-state conditions at higher currents and increased conversion rates [54], and b) the non-uniform primary, secondary and tertiary current density distributions throughout the porous electrodes [55]. The potential and current density vary along the thickness of the flow-through porous structures and electrolyte, decreasing between the membrane and the current collector [56-58]. At the same time, the tertiary current distribution is a function of the distance along the length of the porous electrodes under plug-flow reactor mode of operation [56-58]. Deviations from the ideal response are expected in any electrode of practical dimensions. The same has been observed in graphite felt electrodes due to the potential drop across the material [32].

4.5. Limiting current and enhancement factor

Figure 7a) shows the limiting current density at increasing electrolyte flow rates for different electrodes using chronoamperometry at a potential of +0.2 V *vs.* $Hg|Hg_2SO_{4(satd)}$. The reduction current increases in the following sequence: plate < mesh < felt A < micromesh < felt B < felt C. Evidently, porous electrodes develop higher current densities, discouraging the use of planar electrodes for efficient Ce conversion. The limiting current values for plate, mesh and felt electrodes measured by this method have an excellent agreement (maximum difference of 4%) with those observed in the polarisation curves at the same potential. In contrast, the current values observed in the polarisation curve of the micromesh were higher by *ca*. 10% compared to those by chronoamperometry. In summary, the current measured by chronoamperometry was

more accurate than the observed at polarisation curves and more suitable for determination of $k_m A_e$.

The current observed at the micromesh and felt electrodes increased with mean linear flow velocity according to a power law (Figure 7a). The limiting current of the plate and the mesh electrodes follows an apparent linear relationship before reaching what appears to be underperformance result of flow bypass in the cell indicated by a change of slope (Figure 7a). This takes place at flow velocities over 5 cm s^{-1} for the Pt/Ti mesh ($\varepsilon = 0.71$), while the Pt/Ti plate + ITP ($\varepsilon = 0.78$) shows a similar effect at v >10 cm s^{-1}. The current measured at the micromesh ($\varepsilon = 0.53$) and felts ($\varepsilon = 0.80$) increases following a logarithmic relation. The current at the felt electrodes was directly proportional to the Pt loading (see section 4.1). Consistently, Pt/Ti felt A had a lower Pt loading than the micromesh.

Assuming that k_m does not suffer significant variation with the concentration of electroactive species, the cathodic limiting current density of the cell at other concentrations of Ce(IV) can be estimated at a certain mean linear flow rate using Equation (12). In the case of the Pt/Ti mesh electrode, the expected current density (from projected area) for 0.6 mol dm^{-3} Ce(IV) at 5 cm s^{-1} would be 0.215 A cm^{-2}. For comparison, an industrial electrochemical reactor with a similar mesh electrode operating at 28 cm s^{-1} required an oxidation limiting current of *ca*. 0.25 A cm^{-2} for 1 mol dm^{-3} Ce(III) in MSA assuming an efficiency of 100% [45]. These values are comparable; the higher current in [45] is the result of the higher concentration and flow rate.

The current enhancement factor, β comparing the behaviour of a Pt/Ti planar electrode in an unrestricted channel with other electrodes is shown in Figure 7b). As expected, when highly porous structures are used the value of β is greatly increased. For the mesh, β is between 15

and 20, for the micromesh stack between 52 and 62, and for the felt C between 160 and 108 for increasing electrolyte flow rates. These enhancement values are typical for porous electrodes. The Pt/Ti felt C shows the highest increase in limiting current for a given projected electrode area, although this effect is reduced with increasing mean linear flow velocity of the electrolyte. The plate electrode in combination with an ITP showed values between 2.2 and 3.0, which are similar to the values of the mass transport enhancement factor, γ', reported for turbulence promoters ($\beta = \gamma'$ for planar electrodes), e.g., up to 3.5 [59]. The use of turbulence promoters nearly doubled the current efficiency of anodic Ce(III) oxidation in comparison to flat electrodes in an obsolete process performed in sulfuric acid solutions [50].

The main benefit of a high surface area porous material for a Zn-Ce RFB is the availability of higher operational current densities and reduced voltage efficiency losses. This effect is obvious in the all-vanadium RFB, which uses carbon felt electrodes. Limiting currents are not necessarily achieved in RFBs, since these devices might be charge/discharged at variable currents. Nevertheless, the limiting current at a flow battery provides insight into the mass transport limitations of the cell and electrodes as a function of electrolyte flow velocity.

4.6. Determination of $k_m A_e$ and its empirical correlation to the electrolyte flow rate

The volumetric mass transport coefficient $k_m A_e$ was calculated using Equation (12) from the current measured at the electrodes by chronoamperometry experiments of the type shown in Figure 6b), assuming steady-state mass transport control. A logarithmic-logarithmic plot in Figure 8a) shows $k_m A_e$ as a function of mean linear velocity for the various electrode materials studied. Figure 8b) shows $k_m A_e$ as a function of Reynolds number. The $k_m A_e$ values of the electrodes increase in the sequence: plate (unrestricted channel) < plate + ITP < mesh < felt A < micromesh < felt B < felt C. The values for the empirical constants a' and b' that describe

each electrode are shown in Table 3. In all cases, the value of $k_m A_e$ increases along with the flow rate due to higher mass transport to the electrodes and this is described by the empirical constant b'. Taking the values of a' from Table 3, the Pt/Ti felt C increased the mass transport by 72 times compared to the Pt/Ti plate + ITP and 156 times compared to the Pt/Ti plate in an empty channel. The Pt/Ti micromesh and mesh increased the mass transport by 37 and 3.3 times compared to the Pt/Ti plate + ITP, respectively. The constant a' is related to the active area (Pt coverage) of the electrodes.

The maximum values of $k_m A_e$ are achieved by the Pt/Ti felt C, which has the highest volumetric Pt loading (see section 4.1), followed by the Pt/Ti micromesh stack electrode. These results are in agreement with the literature, e.g., nickel felt produces higher values of $k_m A_e$ than micromesh or foam for ferricyanide ion reduction [30]. The lower performance of Pt/Ti felt A and B is due to their lower Pt content. The values of $k_m A_e$ for the mesh electrode are nearly an order of magnitude lower than those of the micromesh, while the planar electrode gives the lowest values.

The performances of other cells involving cerium conversion are explained by these results. For instance, Harrison *et al*. related mean linear flow velocity and electrode structure (functions of $k_m A_e$) to the current efficiency of industrial Ce(III) oxidation [60]. At a current density of 0.4 A cm^{-2}, a Pt/Ti plate showed a current efficiency of 65% while a Pt/Ti mesh and a double mesh stack showed values of 93% and 99%, respectively; a recognizable behaviour. Those results are a consequence of the increasing values of $k_m A_e$ for such materials. Similarly, Tucker *et al.* have recently observed that fine woven Pt mesh outperforms coarse expanded Pt/Ti mesh in the H_2-Ce_2 fuel cell [24], increasing the current density at which mass transport limitation appears during the cell polarisation. They also noted that increasing the number of stacked Pt

meshes in the electrode, i.e., the extension of the active surface area, increased the maximum power density of the cell.

The consideration of $k_m A_e$ and its empirical description as expressed in Equation (11) allows to circumvent the problems in the determination of k_m in flow cells with porous electrodes that arise from using unmodified dimensionless number correlations of the form shown in Equation (7), which are strictly valid for developed flow in open channel cells, i.e., planar electrodes. For instance, Harrison [45] used these relationships to characterize an industrial flow reactor for Ce(III) oxidation with Pt/Ti mesh (porous) anodes and noted that the limiting current densities estimated from k_m values were unexpectedly inadequate to predict the low current efficiencies at those electrodes.

Studies of $k_m A_e$ are found in the literature for other metallic porous electrodes from limiting current of ferricyanide reduction. In agreement with the higher $k_m A_e$ values yielded by Pt/Ti felt C in comparison to the micromesh, Marrachino *et al.* reported $k_m A_e$ values of 0.81 s^{-1} for Ni felt ($\varepsilon = 0.95$, thickness 1.3 mm) and 0.46 s^{-1} for Ni foam ($\varepsilon = 0.95$, thickness 1.4 mm) at a mean linear flow rate of 4.6 cm s^{-1} [30]. Langlois *et al.* reported the values for the empirical constants that describe $k_m A_e$ for Ni foam electrodes [34]. For instance, for a 100 ppi Ni foam ($\varepsilon = 0.97$, thickness 2.1 mm) in a similar flow configuration a' was 1.18 and b' was 0.47 (converted values to cm s^{-1}). Brown *et al*. reported that Ni foam ($\varepsilon = 0.87$, thickness 4 mm) and a stacked Ni mesh ($\varepsilon = 0.62$, thickness 7.5 mm) had $k_m A_e$ values of 0.09 s^{-1} and 0.19 s^{-1}, respectively, at a mean linear flow velocity of 9 cm s^{-1} in the FM01-LC flow reactor [61]. All of these values are higher than those presented in this work due to more diluted, low-viscosity electrolytes: typically 0.001 mol dm^{-3} $[Fe(CN)_6]^{3-}$, 0.05 mol dm^{-3} $[Fe(CN)_6]^{4-}$ in 0.5 mol dm^{-3}

NaOH or 1.0 mol dm^{-3} KOH. The overall results are similar; porous electrodes of high surface area greatly increase mass transport rates.

Shorter electrolyte flow pathways in porous electrodes can increase $k_m A_e$, as demonstrated for Br_2 [62] and $[Fe(CN)_6]^{4-}$ [32] reduction at carbon felt electrodes. It follows that $k_m A_e$ could be increased significantly if Pt/Ti C felt was used in flow-across configuration with inter-digitated electrolyte channels (similar to a fuel cell), which could also reduce the hydraulic pressure drop across the porous material. This configuration has been adopted in all-vanadium systems, e.g. in [63]. Thinner felts also prevent trapped gas bubbles inside the electrodes observed in thick or dense felt electrodes at low electrolyte flow rates [30,34].

4.7 General considerations

There are several implications of these studies, which merit further research:

- Thin (<0.5 mm), fully platinised felt electrodes could be implemented in flow-across configuration in order to further increase the conversion rate of cerium ions by enhancing mass transport and electrode surface area, while reducing pressure drop, electrode volume and cost in comparison to flow-through electrodes.
- Individual pieces of expanded micromesh could be fully coated before constructing a Pt/Ti micromesh stack electrode, resulting in a robust porous electrode with higher active area that the attained in this work.
- Uniform platinum coating of thin porous titanium substrates could be performed by bipolar electrodeposition in rectangular stirred baths, pulse electrodeposition, chemical vapour deposition or electroless deposition.
- The cathodic corrosion of uncoated titanium in platinised electrodes (e.g., during battery discharge) should be investigated.

5. Conclusions

- The volumetric mass transport coefficient, $k_m A_e$, has been determined for various platinised-titanium electrodes for conversion of cerium ions in MSA. This performance factor can be used to estimate the fractional conversion of the electroactive species and to approximate the dimensions of efficient electrodes.
- The characteristic discharge cell potential of a Zn-Ce RFB using these electrode materials has been explained as the result of mass transport limitations in the positive half-cell. Highly porous materials must be used as positive electrodes in Ce-based RFBs.
- Titanium felt with high degree of platinum coverage provides the highest values of $k_m A_e$. Higher cerium conversion rates might prove useful in anodic generation of Ce(III) for diverse electrochemical applications.
- Platinised-titanium micromesh is more effective as an electrode material than the commercial platinised-titanium expanded mesh currently used in Ce-based RFBs and other electrochemical operations.
- The high potential losses in Ce-based RFBs during discharge and the low conversion efficiency in anodic generation of Ce(III) observed with planar platinised-titanium electrodes is the result of their extremely limited surface area and insufficient mass transport.

Acknowledgements

LFA gratefully acknowledges the financial support of CONACYT and SEP. The Research Institute for Industry (RIFI) of the University of Southampton also provided support for the acquisition of materials. This study forms part of LFA's PhD research programme. All data

supporting this study are openly available from the University of Southampton repository at http://dx.doi.org/10.5258/SOTON/401355.

List of symbols

a	Empirical constant in equation (7)	–
a'	Empirical constant in equation (11)	s^{-1}
A_a	Electrode active area per unit electrode surface	cm^2
A_e	Electrode area per unit electrode volume	cm^{-1}
A	Electrode geometrical area	cm^2
b	Empirical constant in equation (7)	–
b'	Empirical constant in equation (11)	–
B	Breadth of rectangular flow channel	cm
c	Reactant concentration	mol cm^{-3}
d_e	Equivalent diameter of a rectangular flow channel	cm
D	Diffusion coefficient of an aqueous species	$cm^2\ s^{-1}$
E	Electrode potential *vs.* a reference electrode	V
E_{cell}	Cell potential	V
F	Faraday constant	C mol^{-1}
I	Current	A
I_L	Limiting current due to convective-diffusion	A
I_L'	Limiting current due to convective-diffusion at planar electrode	A
j	Current density	A cm^{-2}
k_m	Mass transfer coefficient	cm s^{-1}
$k_m A_e$	Volumetric mass transfer coefficient	s^{-1}
L	Length of rectangular flow channel	cm

n	Amount of a electroactive species	mol
q	Electrical charge	C
Q	Volumetric flow rate of electrolyte	$cm^3\ s^{-1}$
R	Electrical resistance	Ω
R_A	Area-specific resistance	$\Omega\ cm^2$
S	Channel separation between electrode and membrane	cm
t	Time	s
T	Temperature	K
v	Mean linear flow velocity of electrolyte	$cm\ s^{-1}$
V_e	Overall volume of electrode	cm^3
z	Electron stoichiometry	Dimensionless

Greek letters

β	Limiting current enhancement factor in equation (13)	Dimensionless
γ	Aspect ratio of flow channel	Dimensionless
γ'	Mass transport enhancement factor	Dimensionless
ν	Kinematic viscosity of the electrolyte	$cm^2\ s^{-1}$
ε	Volumetric porosity	Dimensionless
ρ	Fluid density	$g\ cm^{-3}$
ω	Angular velocity	$rad\ s^{-1}$

Dimensionless groups

Le	Dimensionless length of a flow channel	Dimensionless
Re	Reynolds number	Dimensionless
Sc	Schmidt number	Dimensionless

Sh	Sherwood number	Dimensionless

References

[1] F.C. Walsh, C. Ponce de León, L. Berlouis, G. Nikiforidis, L.F. Arenas-Martínez, D. Hodgson, D. Hall, The development of Zn-Ce hybrid redox flow batteries for energy storage and their continuing challenges, ChemPlusChem. 80 (2015) 288–311. doi:10.1002/cplu.201402103.

[2] Z. Xie, Q. Liu, Z. Chang, X. Zhang, The developments and challenges of cerium half-cell in zinc–cerium redox flow battery for energy storage, Electrochim. Acta. 90 (2013) 695–704. doi:10.1016/j.electacta.2012.12.066.

[3] P.K. Leung, C. Ponce de León, C.T.J. Low, A.A. Shah, F.C. Walsh, Characterization of a zinc-cerium flow battery, J. Power Sources. 196 (2011) 5174–5185. doi:10.1016/j.jpowsour.2011.01.095.

[4] G. Nikiforidis, L. Berlouis, D. Hall, D. Hodgson, Charge/discharge cycles on Pt and Pt-Ir based electrodes for the positive side of the Zinc-Cerium hybrid redox flow battery, Electrochim. Acta. 125 (2014) 176–182. doi:10.1016/j.electacta.2014.01.075.

[5] P.K. Leung, C. Ponce de León, C.T.J. Low, F.C. Walsh, Zinc deposition and dissolution in methanesulfonic acid onto a carbon composite electrode as the negative electrode reactions in a hybrid redox flow battery, Electrochim. Acta. 56 (2011) 6536–6546. doi:10.1016/j.electacta.2011.04.111.

[6] G. Nikiforidis, L. Berlouis, D. Hall, D. Hodgson, A study of different carbon composite materials for the negative half-cell reaction of the zinc cerium hybrid redox flow cell, Electrochim. Acta. 113 (2013) 412–423. doi:10.1016/j.electacta.2013.09.061.

[7] P.K. Leung, C. Ponce de León, F.C. Walsh, An undivided zinc–cerium redox flow battery operating at room temperature (295 K), Electrochem. Commun. 13 (2011) 770–773. doi:10.1016/j.elecom.2011.04.011.

[8] Z. Xie, F. Xiong, D. Zhou, Study of the Ce^{3+}/Ce^{4+} redox couple in mixed-acid media (CH_3SO_3H and H_2SO_4) for redox flow battery application, Energy Fuels. 25 (2011) 2399–2404. doi:10.1021/ef200354b.

[9] F. Xiong, D. Zhou, Z. Xie, Y. Chen, A study of the Ce^{3+}/Ce^{4+} redox couple in sulfamic acid for redox battery application, Applied Energy. 99 (2012) 291–296. doi:10.1016/j.apenergy.2012.05.021.

[10] G. Nikiforidis, W.A. Daoud, Effect of mixed acid media on the positive side of the hybrid zinc-cerium redox flow battery, Electrochim. Acta. 141 (2014) 255–262. doi:10.1016/j.electacta.2014.06.142.

[11] P.K. Leung, C. Ponce de León, F.J. Recio, P. Herrasti, F.C. Walsh, Corrosion of the zinc negative electrode of zinc–cerium hybrid redox flow batteries in methanesulfonic acid, J. Appl. Electrochem. 44 (2014) 1025–1035. doi:10.1007/s10800-014-0714-y.

[12] L.F. Arenas, F.C. Walsh, C. Ponce de León, The importance of cell geometry and

electrolyte properties to the cell potential of Zn-Ce hybrid flow batteries, J. Electrochem. Soc. 163 (2016) A5170–A5179. doi:10.1149/2.0261601jes.

[13] R. Zito, Energy Storage: A New Approach, John Wiley & Sons, Hoboken (NJ), 2010.

[14] P.K. Leung, C. Ponce de León, F.C. Walsh, The influence of operational parameters on the performance of an undivided zinc–cerium flow battery, Electrochim. Acta. 80 (2012) 7–14. doi:10.1016/j.electacta.2012.06.074.

[15] B. Fang, S. Iwasa, Y. Wei, T. Arai, M. Kumagai, A study of the Ce(III)/Ce(IV) redox couple for redox flow battery application, Electrochim. Acta. 47 (2002) 3971–3976.

[16] Y. Liu, X. Xia, H. Liu, Studies on cerium (Ce^{4+}/Ce^{3+})–vanadium(V^{2+}/V^{3+}) redox flow cell—cyclic voltammogram response of Ce^{4+}/Ce^{3+} redox couple in H_2SO_4 solution, J. Power Sources. 130 (2004) 299–305. doi:10.1016/j.jpowsour.2003.12.017.

[17] K.M. Govindan, I.S. Moon, Evaluation of dual electrochemical cell design for cerium-vanadium redox flow battery to use different combination of electrodes, Int J Electrochem Sci. (2013).

[18] V. Amstutz, K.E. Toghill, F. Powlesland, H. Vrubel, C. Comninellis, X. Hu, H.H. Girault, Renewable hydrogen generation from a dual-circuit redox flow battery, Energy Environ. Sci. 7 (2014) 2350–2358. doi:10.1039/C4EE00098F.

[19] P.K. Leung, M.R. Mohamed, A.A. Shah, Q. Xu, M.B. Conde-Duran, A mixed acid based vanadium–cerium redox flow battery with a zero-gap serpentine architecture, J. Power Sources. 274 (2015) 651–658. doi:10.1016/j.jpowsour.2014.10.034.

[20] N.D. Mota, D.A. Finkelstein, J.D. Kirtland, C.A. Rodriguez, A.D. Stroock, H.D. Abruña, Membraneless, room-temperature, direct borohydride/cerium fuel cell with power density of over 0.25 W/cm^2, J. Am. Chem. Soc. 134 (2012) 6076–6079. doi:10.1021/ja211751k.

[21] Z. Na, S. Xu, D. Yin, L. Wang, A cerium-lead redox flow battery system employing supporting electrolyte of methanesulfonic acid, 295 (2015) 28–32. doi:10.1016/j.jpowsour.2015.06.115.

[22] H.M.H. Dewage, B. Wu, A. Tsoi, V. Yufit, G.J. Offer, N. Brandon, A novel regenerative hydrogen cerium fuel cell for energy storage applications, J. Mater. Chem. A. 3 (2015) 9446–9450. doi:10.1039/C5TA00571J.

[23] M.C. Tucker, A. Weiss, A.Z. Weber, Cerium-hydrogen redox flow cell optimization, Meet. Abstr. MA2016-01 (2016) 379–379.

[24] M.C. Tucker, A. Weiss, A.Z. Weber, Improvement and analysis of the hydrogen-cerium redox flow cell, J. Power Sources. 327 (2016) 591–598. doi:10.1016/j.jpowsour.2016.07.105.

[25] F. Coeuret, A. Storck, Eléments de Génie Électrochimique, 2nd ed., Éditions TEC et DOC / Lavoisier, 1993.

[26] C. Ponce de León, G.W. Reade, I. Whyte, S.E. Male, F.C. Walsh, Characterization of the reaction environment in a filter-press redox flow reactor, Electrochim. Acta. 52 (2007) 5815–5823. doi:10.1016/j.electacta.2007.02.080.

[27] L.F. Arenas, C. Ponce de León, F.C. Walsh, Electrochemical redox processes involving soluble cerium species, Electrochim. Acta. 205 (2016) 226–247. doi:10.1016/j.electacta.2016.04.062.

[28] F.C. Walsh, A First Course on Electrochemical Engineering, The Electrochemical Consultancy, Romsey, 1993.

[29] D. Pletcher, F.C. Walsh, Three-dimensional electrodes, in: D. Gernders, N. Weinberg (Eds.), Electrochemistry for a Cleaner Environment, The Electrosynthesis Company, New York, 1992: pp. 51–100.

[30] J.M. Marracino, F. Coeuret, S. Langlois, A first investigation of flow-through porous electrodes made of metallic felts or foams, Electrochim. Acta. 32 (1987) 1303–1309. doi:10.1016/0013-4686(87)85059-4.

[31] H. Zhou, H. Zhang, P. Zhao, B. Yi, A comparative study of carbon felt and activated carbon based electrodes for sodium polysulfide/bromine redox flow battery, Electrochim. Acta. 51 (2006) 6304–6312. doi:10.1016/j.electacta.2006.03.106.

[32] B. Delanghe, S. Tellier, M. Astruc, Mass transfer to a carbon or graphite felt electrode, Electrochim. Acta. 35 (1990) 1369–1376. doi:10.1016/0013-4686(90)85008-B.

[33] P. Trinidad, F.C. Walsh, Batch oxidation of cerous ions in a divided FM01-LC filter-press reactor, Icheme Symposium Series. 145 (1999) 281–290.

[34] S. Langlois, F. Coeuret, Flow-through and flow-by porous electrodes of nickel foam. II. Diffusion-convective mass transfer between the electrolyte and the foam, J. Appl. Electrochem. 19 (1989) 51–60. doi:10.1007/BF01039389.

[35] A. Frías-Ferrer, J. González-García, V. Sáez, C. Ponce de León, F.C. Walsh, The effects of manifold flow on mass transport in electrochemical filter-press reactors, AIChE J. 54 (2008) 811–823. doi:10.1002/aic.11426.

[36] J.L. Nava, M.T. Oropeza, C. Ponce de León, J. González-García, A.J. Frías-Ferrer, Determination of the effective thickness of a porous electrode in a flow-through reactor; effect of the specific surface area of stainless steel fibres, used as a porous cathode, during the deposition of Ag(I) ions, Hydrometallurgy. 91 (2008) 98–103. doi:10.1016/j.hydromet.2007.12.001.

[37] G. Coria, T. Pérez, I. Sirés, J.L. Nava, Mass transport studies during dissolved oxygen reduction to hydrogen peroxide in a filter-press electrolyzer using graphite felt, reticulated vitreous carbon and boron-doped diamond as cathodes, J. Electroanal. Chem. 757 (2015) 225–229. doi:10.1016/j.jelechem.2015.09.031.

[38] P. Trinidad, C. Ponce de León, F.C. Walsh, The use of electrolyte redox potential to monitor the Ce(IV)/Ce(III) couple, J. Environ. Manage. 88 (2008) 1417–1425. doi:10.1016/j.jenvman.2007.07.007.

[39] C.H. Angell, Surface treatment of titanium, US patent 3,650,861, 1972.

[40] M.E. Baumgärter, C.J. Raub, The electrodeposition of platinum and platinum alloys, Platinum Metals Rev. 32 (1988) 188–197.

[41] F. Feigl, V. Anger, Spot Tests in Inorganic Analysis, 6 ed., Elsevier, Amsterdam, 2012.

[42] L.F. Arenas, C. Ponce de León, F.C. Walsh, *in progress*.

[43] G. Nikiforidis, L. Berlouis, D. Hall, D. Hodgson, An electrochemical study on the positive electrode side of the zinc–cerium hybrid redox flow battery, Electrochim. Acta. 115 (2014) 621–629. doi:10.1016/j.electacta.2013.09.081.

[44] R.M. Spotnitz, R.P. Kreh, J.T. Lundquist, P.J. Press, Mediated electrosynthesis with cerium (IV) in methanesulphonic acid, J. Appl. Electrochem. 20 (1990) 209–215.

[45] S. Harrison, Hydro-Quebec, Indirect cerium mediated electrosynthesis, US patent 5,516,407, 1996.

[46] J.M. Nzikou, M. Aurousseau, F. Lapicque, Electrochemical investigations of the Ce(III)/Ce(IV) couple related to a Ce(IV)-assisted process for SO_2/NO_x abatement, J. Appl. Electrochem. 25 (1995) 967–972. doi:10.1007/BF00241592.

[47] G. Nikiforidis, L. Berlouis, D. Hall, D. Hodgson, Impact of electrolyte composition on the performance of the zinc-cerium redox flow battery system, J. Power Sources. 243 (2013) 691–698. doi:10.1016/j.jpowsour.2013.06.045.

[48] F. Hine, K. Murakami, Bubble effects on the solution IR drop in a vertical electrolyzer under free and forced convection, J. Electrochem. Soc. 127 (1980) 292–297. doi:10.1149/1.2129658.

[49] J. Eigeldinger, H. Vogt, The bubble coverage of gas-evolving electrodes in a flowing electrolyte, Electrochim. Acta. 45 (2000) 4449–4456. doi:10.1016/S0013-4686(00)00513-2.

[50] I.M. Dalrymple, J.P. Millington, An indirect electrochemical process for the production of naphthaquinone, J. Appl. Electrochem. 16 (1986) 885–893. doi:10.1007/BF01006534.

[51] S. Slade, S.A. Campbell, T.R. Ralph, F.C. Walsh, Ionic conductivity of an extruded Nafion 1100 EW series of membranes, J. Electrochem. Soc. 149 (2002) A1556–A1564. doi:10.1149/1.1517281.

[52] D. Aaron, Z. Tang, A.B. Papandrew, T.A. Zawodzinski, Polarization curve analysis of all-vanadium redox flow batteries, J. Appl. Electrochem. 41 (2011) 1175–1182. doi:10.1007/s10800-011-0335-7.

[53] P. Zhao, H. Zhang, H. Zhou, B. Yi, Nickel foam and carbon felt applications for sodium polysulfide/bromine redox flow battery electrodes, Electrochim. Acta. 51 (2005) 1091–1098. doi:10.1016/j.electacta.2005.06.008.

[54] J.R. Selman, C.W. Tobias, Mass-transfer measurements by the limiting-current technique, in: Advances in Chemical Engineering Volume 10, Elsevier, 1978: pp. 211–318.

[55] J. Newman, K.E. Thomas-Alyea, Electrochemical Systems, 3rd Ed., John Wiley & Sons, Hoboken (NJ), 2004.

[56] S. Langlois, F. Coeuret, Flow-through and flow-by porous electrodes of nickel foam Part III: theoretical electrode potential distribution in the flow-by configuration, J. Appl. Electrochem. 20 (1990) 740–748. doi:10.1007/BF01094300.

[57] A.I. Masliy, N.P. Poddubny, A.Z. Medvedev, V.O. Lukyanov, Analysis of the distribution of geometrical current density along the direction of solution flow inside flow-by porous electrodes, J. Electroanal. Chem. 757 (2015) 128–136.

[58] A.I. Maslii, N.P. Poddubnyi, A.Z. Medvedev, Distribution of geometrical current density inside a flow-by porous electrode: Effect of electrode parameters and electrochemical reactions, Russ. J. Electrochem. 52 (2016) 576–583.

[59] C.J. Brown, F.C. Walsh, D. Pletcher, Mass transfer and pressure drop in a laboratory filterpress electrolyser, Trans. IChemE. 73 (1995) 196–205.

[60] S. Harrison, A. Théorêt, The electrosynthesis of naphthoquinone and tetrahydroanthraquinone, J. New Mat. Electrochem. Systems. 2 (1999) 1–9.

[61] C.J. Brown, D. Pletcher, F.C. Walsh, J.K. Hammond, D. Robinson, Studies of three-dimensional electrodes in the FMO1-LC laboratory electrolyser, J. Appl. Electrochem. 24 (1994) 95–106. doi:10.1007/BF00247779.

[62] K. Kinoshita, S.C. Leach, Mass-transfer study of carbon felt, flow-through electrode, J. Electrochem. Soc. 129 (1982) 1993–1997. doi:10.1149/1.2124338.

[63] D.S. Aaron, Q. Liu, Z. Tang, G.M. Grim, A.B. Papandrew, A. Turhan, T.A. Zawodzinski, Dramatic performance gains in vanadium redox flow batteries through modified cell architecture, J. Power Sources. 206 (2012) 450–453. doi:10.1016/j.jpowsour.2011.12.026.

Tables

Table 1. Properties of the electrolyte for reaction environment characterization.

Property	Value
Ce(III) methanesulfonate concentration, [Ce(III)]	0.7 mol dm^{-3}
Ce(IV) methanesulfonate concentration, [Ce(IV)]	0.1 mol dm^{-3}
Diffusion coefficient of Ce(IV) ions, $D_{Ce(IV)}$	8.6±0.9 × 10^{-7} cm^2 s^{-1}
Dynamic viscosity, μ	5.3 × 10^{-2} g cm^{-1} s^{-1}
Fluid density, ρ	1.37 g cm^{-3}
Kinematic viscosity, ν	3.9 × 10^{-2} cm^2 s^{-1}
MSA concentration, [MSA]	4.0 mol dm^{-3}
Schmidt number, Sc	45348
Temperature, T	298.2 K

Table 2. Characteristics of the positive electrodes and their respective flow channels.

Electrode	Length, L / cm	Breadth, B / cm	Height, S / cm	Aspect ratio, γ	Equivalent diameter, d_e / cm	Volumetric porosity, ε	Projected area, A / cm^2	Cross-sectional area, A_x / cm^2	Volume, V_e / cm^3
Pt/Ti plate + ITP	6.0	4.0	0.355	0.089	0.652	0.78	24.0	1.42	8.52
Pt/Ti mesh	6.0	4.2	0.740	0.176	1.258	0.71	25.2	3.11	18.7
Pt/Ti micromesh	6.0	4.0	0.255	0.064	0.479	0.53	24.0	1.02	6.24
Pt/Ti felt (A, B and C)	6.0	4.0	0.36	0.090	0.661	0.80	24.0	1.44	8.64

Table 3. Constants describing the performance of Pt/Ti porous electrodes in an industrial-type MSA electrolyte according to the power law, $k_m A_e = a' v^{b'}$. From current data of 0.1 mol dm^{-3} Ce(IV) reduction in 4.0 mol dm^{-3} MSA.

Electrode	a'	b'
Pt/Ti plate (2-D)	3.09×10^{-4}	0.386
Pt/Ti plate + ITP	6.70×10^{-4}	0.526
Pt/Ti mesh	2.24×10^{-3}	0.492
Pt/Ti micromesh	2.48×10^{-2}	0.385
Pt/Ti felt A	1.57×10^{-2}	0.211
Pt/Ti felt B	2.65×10^{-2}	0.248
Pt/Ti felt C	4.82×10^{-2}	0.286

Figure Captions

Figure 1. a) Electrochemical flow cell components and b) experimental arrangement for half-cell measurements of limiting current at Pt/Ti electrodes.

Figure 2. Evaluated Pt/Ti electrode structures: a) plate, b) mesh, c) micromesh d) felt C.

Figure 3. SEM images of the macroscopic structure of the Pt/Ti electrodes studied: a) plate, b) mesh, c) micromesh, d) felt C.

Figure 4. Cyclic voltammetry showing the behaviour of cerium ions in a typical electrolyte for the Zn-Ce RFB. The electrolyte contains 0.8 mol dm^{-3} Ce(III) in 4 mol dm^{-3} MSA at 298.2 K.

Figure 5. Initial cell potential of a Zn-Ce RFB unit cell as a function of applied discharge current density for different positive electrodes: a) Pt/Ti plate, b) Pt/Ti mesh, c) Pt/Ti micromesh, d) Pt/Ti felt C. SOC: 50%, equivalent to an electrolyte composition of 0.4 mol dm^{-3} Ce(IV) + 0.4 mol dm^{-3} Ce(III) in 4 mol dm^{-3} MSA. Temperature: 323.2 K.

Figure 6. a) Polarization curves and b) limiting current measured by chronoamperometry at +0.2 V vs. $Hg|Hg_2SO_{4(satd)}$ for the reduction of Ce(IV) at the Pt/Ti plate + ITP electrode as a function of mean linear electrolyte velocity. Electrolyte composition: 0.1 mol dm^{-3} Ce(IV) + 0.7 mol dm^{-3} Ce(III) in 4 mol dm^{-3} MSA at 298.2 K.

Figure 7. a) Limiting current density for reduction of Ce(IV) ions and b) limiting current enhancement factor *vs*. electrolyte mean linear velocity for different Pt/Ti electrode materials. Current obtained by chronoamperometry at +0.2 V *vs*. $Hg|Hg_2SO_{4(satd)}$. Electrolyte composition: 0.1 mol dm^{-3} Ce(IV) + 0.7 mol dm^{-3} Ce(III) in 4 mol dm^{-3} MSA at 298.2 K.

Figure 8. Logarithmic-logarithmic plot of electrode performance factor $k_m A_e$ for Ce(IV)reduction as a function of a) electrolyte mean linear velocity, b) Reynolds number for different electrode materials. Electrolyte composition: 0.1 mol dm^{-3} Ce(IV) + 0.7 mol dm^{-3} Ce(III) in 4 mol dm^{-3} MSA at 298.2 K.

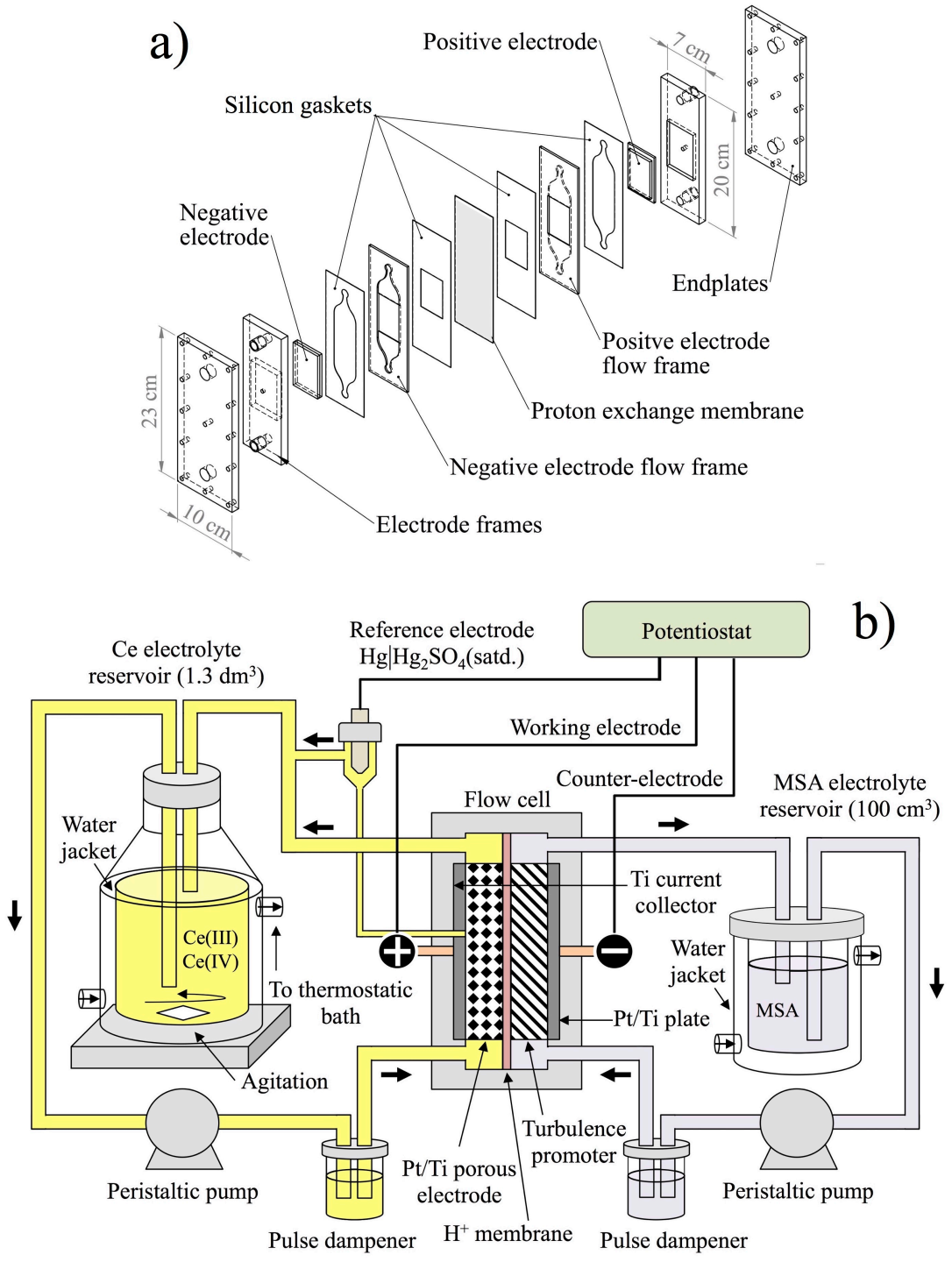
a)
Positive electrode
7 cm
Silicon gaskets
20 cm
Negative electrode
Endplates
Positve electrode flow frame
Proton exchange membrane
23 cm
Negative electrode flow frame
10 cm
Electrode frames
b)
Potentiostat
Reference electrode Hg|Hg2SO4(satd.)
Ce electrolyte reservoir (1.3 dm3)
Working electrode
Counter-electrode
Flow cell
MSA electrolyte reservoir (100 cm3)
Water jacket
Ti current collector
Ce(III) Ce(IV)
To thermostatic bath
Water jacket
MSA
Pt/Ti plate
Agitation
Turbulence promoter
Peristaltic pump
Pt/Ti porous electrode
Peristaltic pump
Pulse dampener
H+ membrane
Pulse dampener

Figure 1.

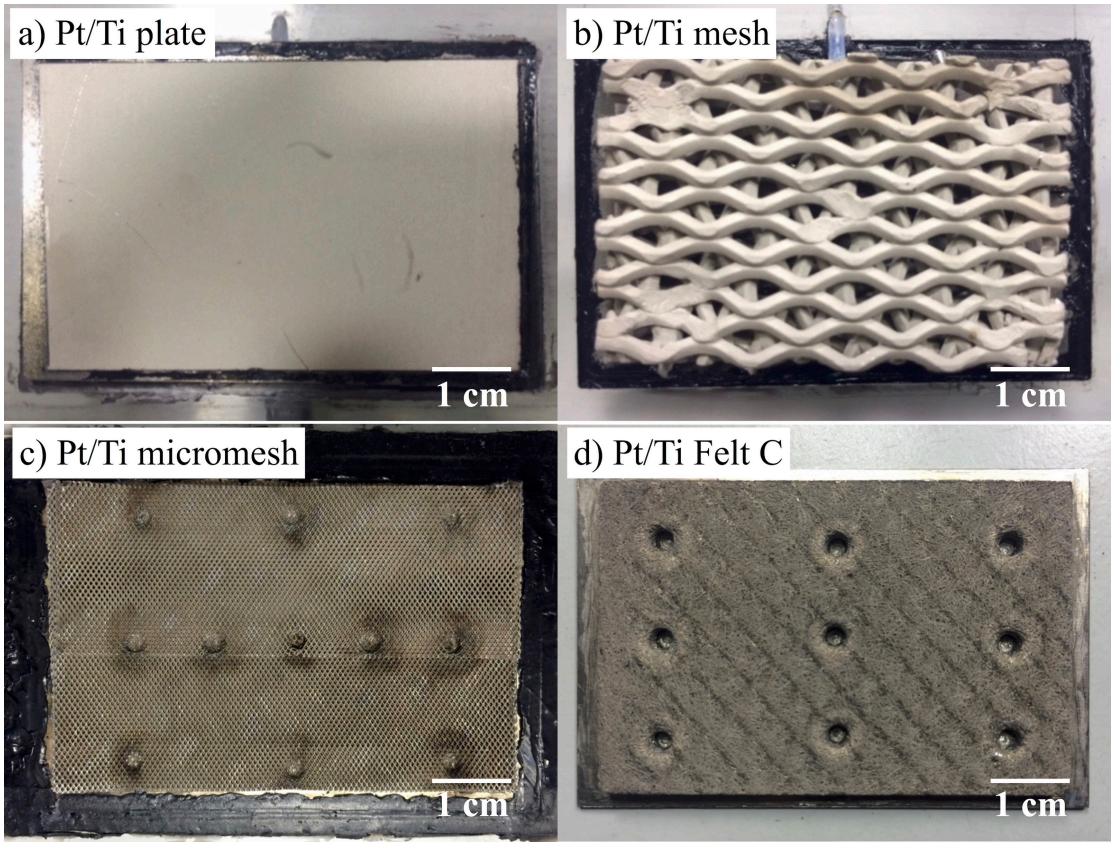
a) Pt/Ti plate
1 cm
b) Pt/Ti mesh
1 cm
c) Pt/Ti micromesh
1 cm
d) Pt/Ti Felt C
1 cm

Figure 2.

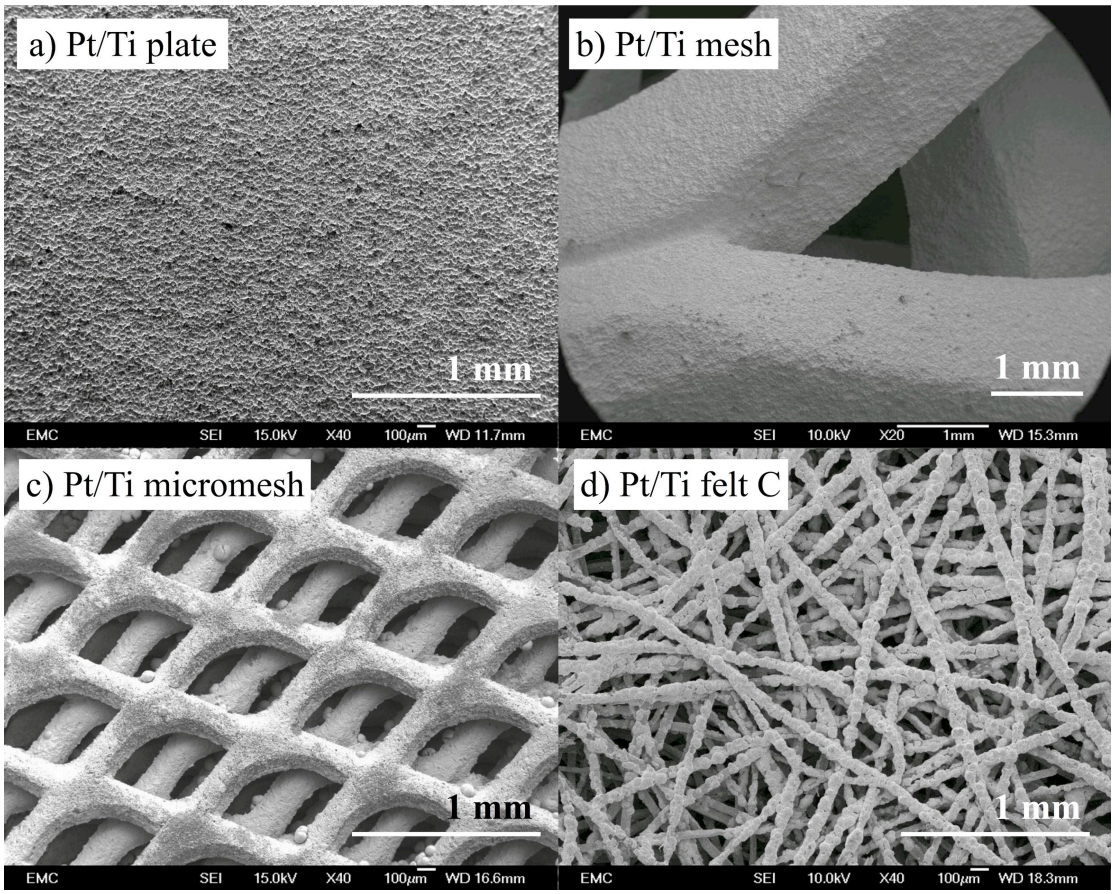
a) Pt/Ti plate
1 mm
EMC SEI 15.0kV X40 100μm WD 11.7mm
b) Pt/Ti mesh
1 mm
EMC SEI 10.0kV X20 1mm WD 15.3mm
c) Pt/Ti micromesh
1 mm
EMC SEI 15.0kV X40 100μm WD 16.6mm
d) Pt/Ti felt C
1 mm
EMC SEI 10.0kV X40 100μm WD 18.3mm

Figure 3.

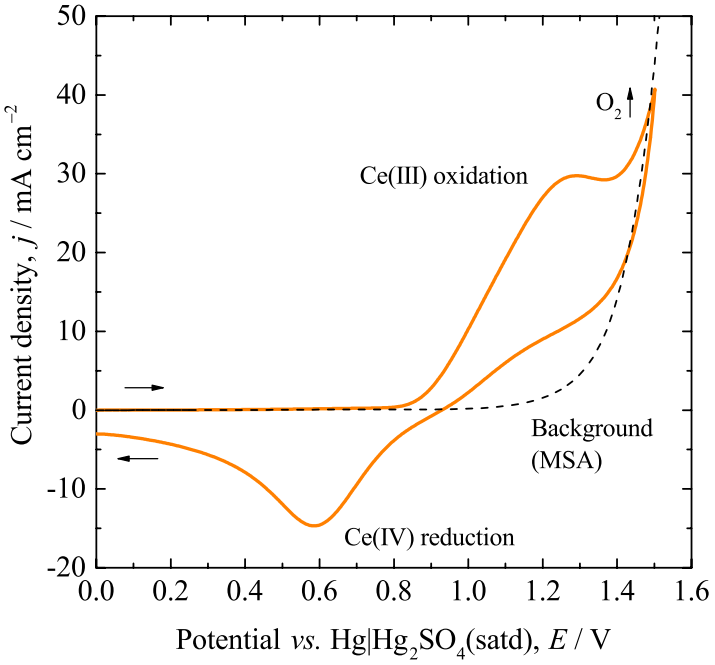
50
40
30
20
10
0
-10
-20
0.0
0.2
0.4
0.6
0.8
1.0
1.2
1.4
1.6
Current density, j / mA cm^{-2}
Potential vs. Hg|Hg$_2$SO$_4$(satd), E / V
O$_2$
Ce(III) oxidation
Background
(MSA)
Ce(IV) reduction

Figure 4.

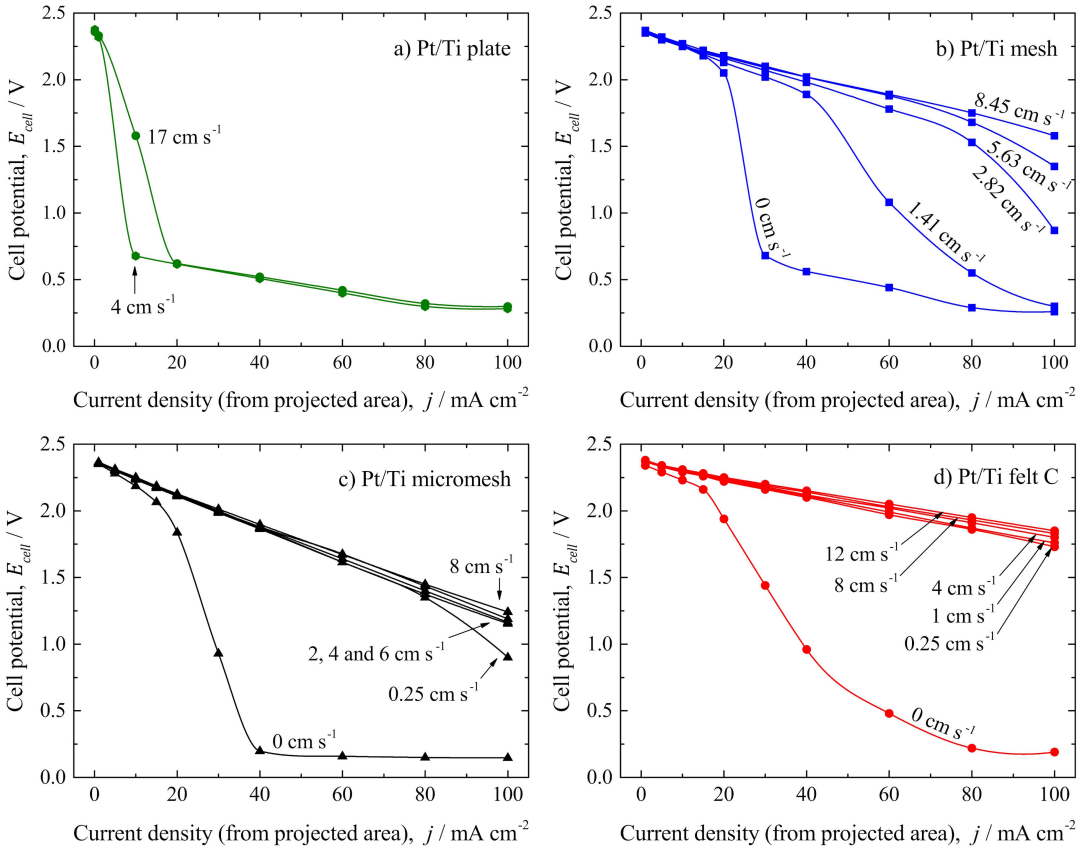
a) Pt/Ti plate
17 cm s-1
4 cm s-1
b) Pt/Ti mesh
8.45 cm s-1
5.63 cm s-1
2.82 cm s-1
1.41 cm s-1
0 cm s-1
c) Pt/Ti micromesh
8 cm s-1
2, 4 and 6 cm s-1
0.25 cm s-1
0 cm s-1
d) Pt/Ti felt C
12 cm s-1
8 cm s-1
4 cm s-1
1 cm s-1
0.25 cm s-1
0 cm s-1
Cell potential, Ecell / V
Current density (from projected area), j / mA cm-2

Figure 5.

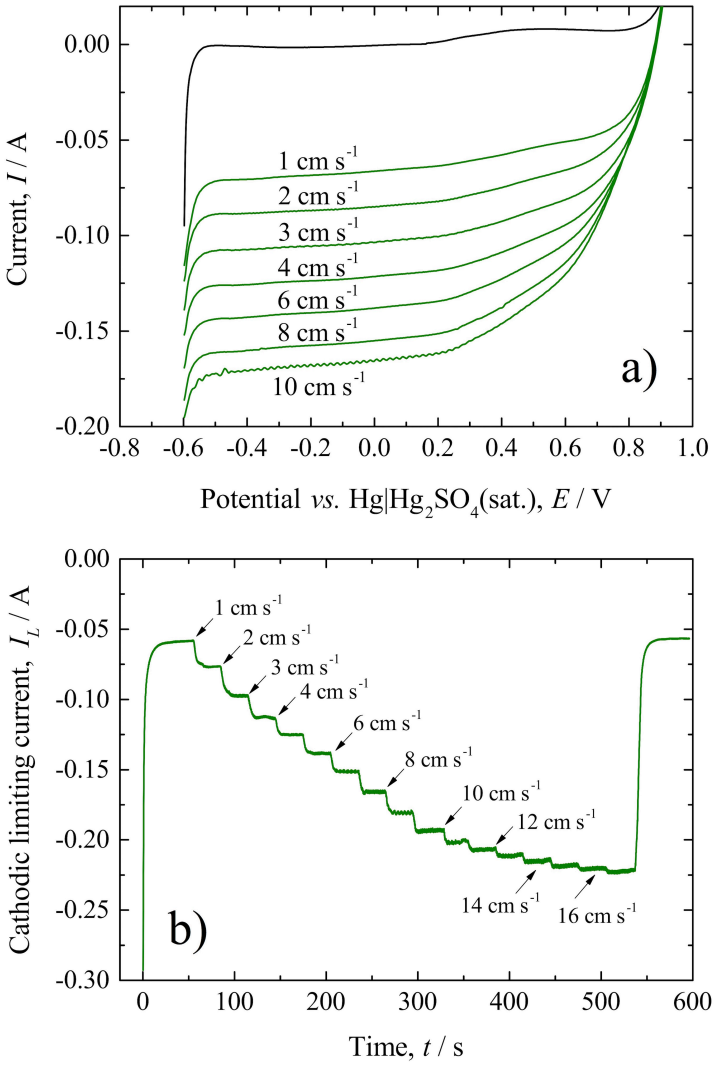
0.00
-0.05
-0.10
-0.15
-0.20
Current, I / A
1 cm s-1
2 cm s-1
3 cm s-1
4 cm s-1
6 cm s-1
8 cm s-1
10 cm s-1
a)
-0.8
-0.6
-0.4
-0.2
0.0
0.2
0.4
0.6
0.8
1.0
Potential vs. Hg|Hg2SO4(sat.), E / V
0.00
-0.05
-0.10
-0.15
-0.20
-0.25
-0.30
Cathodic limiting current, IL / A
1 cm s-1
2 cm s-1
3 cm s-1
4 cm s-1
6 cm s-1
8 cm s-1
10 cm s-1
12 cm s-1
14 cm s-1
16 cm s-1
b)
0
100
200
300
400
500
600
Time, t / s

Figure 6.

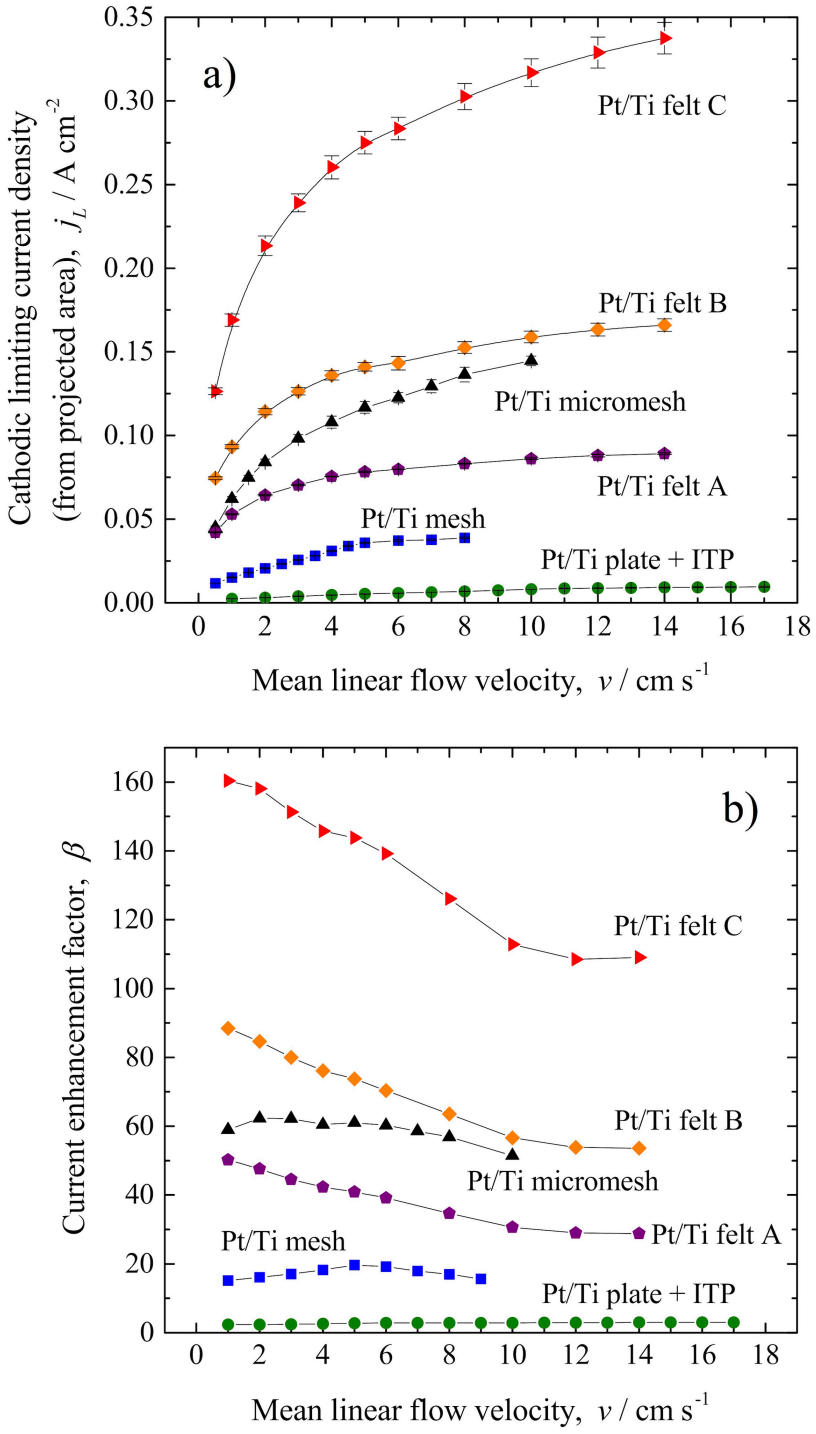
a)
Pt/Ti felt C
Pt/Ti felt B
Pt/Ti micromesh
Pt/Ti felt A
Pt/Ti mesh
Pt/Ti plate + ITP
Cathodic limiting current density
(from projected area), j_L / A cm^{-2}
Mean linear flow velocity, v / cm s^{-1}
b)
Pt/Ti felt C
Pt/Ti felt B
Pt/Ti micromesh
Pt/Ti felt A
Pt/Ti mesh
Pt/Ti plate + ITP
Current enhancement factor, β
Mean linear flow velocity, v / cm s^{-1}

Figure 7.

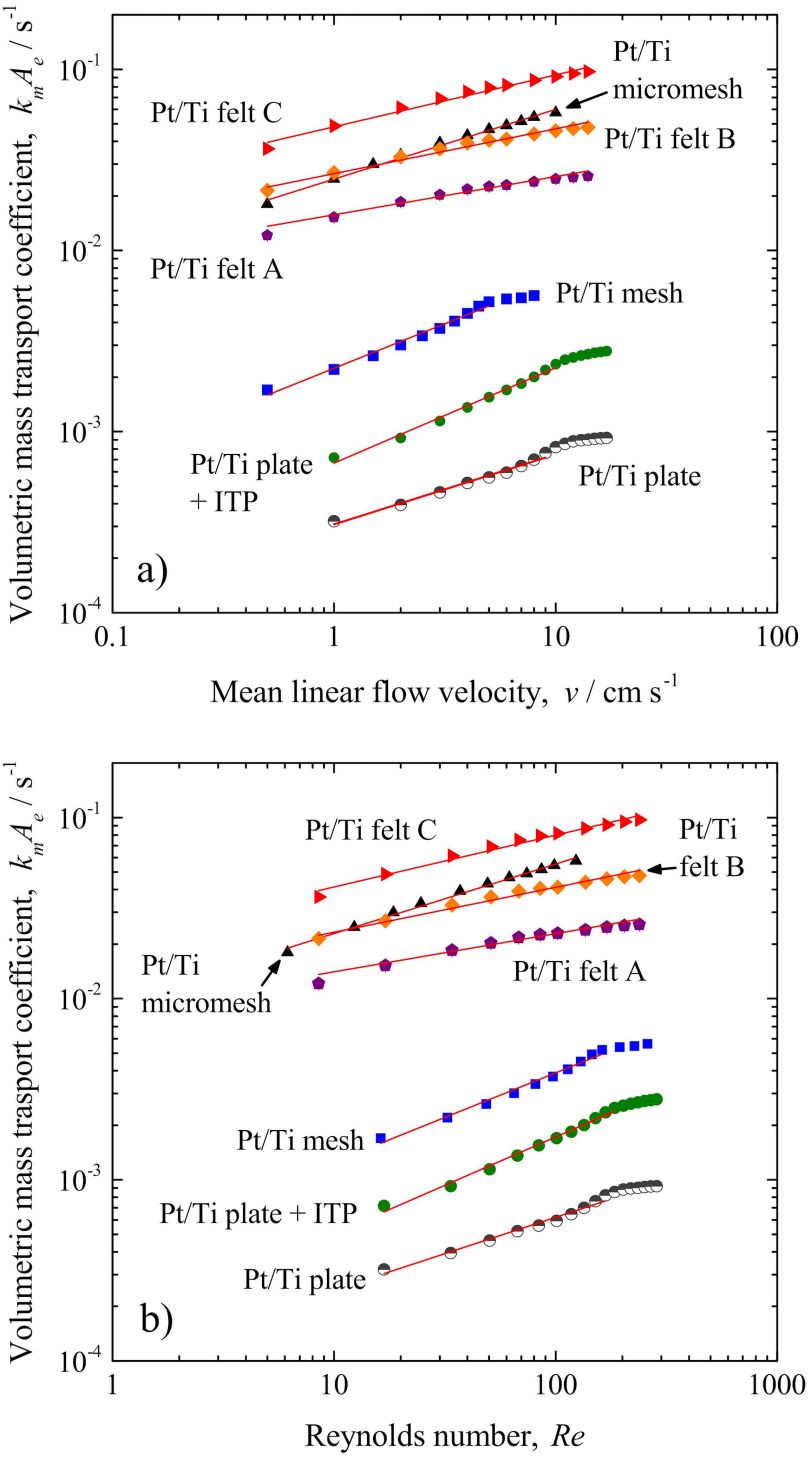
Volumetric mass transport coefficient, $k_m A_e$ / s^{-1}
Pt/Ti felt C
Pt/Ti micromesh
Pt/Ti felt B
Pt/Ti felt A
Pt/Ti mesh
Pt/Ti plate + ITP
Pt/Ti plate
a)
Mean linear flow velocity, v / cm s^{-1}
Volumetric mass trasport coefficient, $k_m A_e$ / s^{-1}
Pt/Ti felt C
Pt/Ti felt B
Pt/Ti micromesh
Pt/Ti felt A
Pt/Ti mesh
Pt/Ti plate + ITP
Pt/Ti plate
b)
Reynolds number, Re

Figure 8.